Ultrasensitive and stable X-ray detection using zero-dimensional lead-free perovskites

Xiaojia Zheng, Wei Zhao, Peng Wang, Hairen Tan, Makhsud I. Saidaminov, Shujie Tie, Ligao Chen, Yufei Peng, Jidong Long, & Wen-Hua Zhang

March 2020

This article was originally published at:
https://doi.org/10.1016/j.jechem.2020.02.049

Citation for this paper:

Zheng, X., Zhao, W., Wang, P., Tan, H., Saidaminov, M. I., Tie, S., Chen, L., Peng, Y., Long, J., & Zhang, W. (2020). Ultrasensitive and stable X-ray detection using zero-dimensional lead-free perovskites. *Journal of Energy Chemistry*, Vol. 49, 299-306. https://doi.org/10.1016/j.jechem.2020.02.049.

Journal of Energy Chemistry 49 (2020) 299–306

Contents lists available at ScienceDirect

Journal of Energy Chemistry

journal homepage: www.elsevier.com/locate/jechem

http://www.journals.elsevier.com/journal-of-energy-chemistry/

Ultrasensitive and stable X-ray detection using zero-dimensional lead-free perovskites

Xiaojia Zheng[a,1], Wei Zhao[b,1], Peng Wang[a,1], Hairen Tan[c], Makhsud I. Saidaminov[d], Shujie Tie[a], Ligao Chen[b], Yufei Peng[b], Jidong Long[b,*], Wen-Hua Zhang[a,**]

[a] Sichuan Research Center of New Materials, Institute of Chemical Materials, China Academy of Engineering Physics, Chengdu 610200, Sichuan, China
[b] Institute of Fluid Physics, China Academy of Engineering Physics, Mianyang 621900, Sichuan, China
[c] National Laboratory of Solid State Microstructures, Jiangsu Key Laboratory of Artificial Functional Materials, College of Engineering and Applied Sciences, Nanjing University, Nanjing 210093, Jiangsu, China
[d] Departments of Chemistry and Electrical & Computer Engineering, Centre for Advanced Materials and Related Technologies (CAMTEC), University of Victoria, Victoria V8P 5C2, BC, Canada

ARTICLE INFO

Article history:
Received 20 February 2020
Revised 27 February 2020
Accepted 27 February 2020
Available online 7 March 2020

Keywords:
X-ray detector
Zero-dimensional perovskite
Lead-free
Carrier concentration
Stability
Limit of detection
Sensitivity

ABSTRACT

Sensitive and reliable X-ray detectors are essential for medical radiography, industrial inspection and security screening. Lowering the radiation dose allows reduced health risks and increased frequency and fidelity of diagnostic technologies for earlier detection of disease and its recurrence. Three-dimensional (3D) organic–inorganic hybrid lead halide perovskites are promising for direct X-ray detection – they show improved sensitivity compared to conventional X-ray detectors. However, their high and unstable dark current, caused by ion migration and high dark carrier concentration in the 3D hybrid perovskites, limits their performance and long-term operation stability. Here we report ultrasensitive, stable X-ray detectors made using zero-dimensional (0D) methylammonium bismuth iodide perovskite ($MA_3Bi_2I_9$) single crystals. The 0D crystal structure leads to a high activation energy (E_a) for ion migration (0.46 eV) and is also accompanied by a low dark carrier concentration (~ 10^6 cm^{-3}). The X-ray detectors exhibit sensitivity of 10,620 μC $Gy_{air}{}^{-1}$ cm^{-2}, a limit of detection (LoD) of 0.62 nGy_{air} s^{-1}, and stable operation even under high applied biases; no deterioration in detection performance was observed following sensing of an integrated X-ray irradiation dose of ~23,800 mGy_{air}, equivalent to > 200,000 times the dose required for a single commercial X-ray chest radiograph. Regulating the ion migration channels and decreasing the dark carrier concentration in perovskites provide routes for stable and ultrasensitive X-ray detectors.

1. Introduction

X-ray detection is widely applied in medical diagnostics and security screening. These applications require sensitive X-ray detectors that enable decreasing the dose required in order to reduce health risks [1,2]. However, the sensitivity and minimum detectable dose rate, or limit of detection (LoD) of X-ray radiological instruments, is limited today by the materials used in the detectors [3]. The sensitivities of direct-conversion amorphous selenium (a-Se) detectors, and of indirect-conversion thallium-doped cesium iodide (CsI:TI) detectors, two dominant X-ray detectors, are lower than 400 μC $Gy_{air}{}^{-1}$ cm^{-2} [4–6].

Enhancing the X-ray sensitivity and lowering the LoD of direct-conversion X-ray detectors has been explored extensively [5]. Organic-inorganic hybrid lead halide perovskites, widely investigated in solar energy conversion, are also promising materials for X-ray detection applications because of their high attenuation coefficients, large mobility-lifetime ($\mu\tau$) products, and their fabrication via solution processing [7–10]. An X-ray sensitivity exceeding 10,000 μC $Gy_{air}{}^{-1}$ cm^{-2} and achieving a LoD of 36 nGy_{air} s^{-1} has been achieved using 3D hybrid perovskite detectors – and both the sensitivity and LoD are superior to those of traditional X-ray detectors [2,11]. However, long-term operational stability in lead halide perovskite X-ray detectors remains to be achieved. Ion migration in 3D hybrid perovskites causes instability and dark current drift, the latter preventing achievement of a low LoD [12,13]. It remains an open problem to achieve X-ray sensitive materials that simultaneously provide high sensitivity, low LoD, and stable detector operation.

---

[*] Corresponding authors.
E-mail addresses: longjidong@tsinghua.org.cn (J. Long), whzhang@caep.cn (W.-H. Zhang).
[1] These authors contributed equally to this work.

https://doi.org/10.1016/j.jechem.2020.02.049
2095-4956/

We posited that disconnecting the inorganic octahedral units in hybrid perovskites could beneficially disrupt ion migration channels. The 0D structure, in which the inorganic octahedral units are disconnected in all directions, enables this goal. 0D compounds also provide more localized electronic structures, which can decrease the dark carrier concentration compared to in 3D or 2D counterparts [14,15]. Suppressing ion migration and lowering dark carrier concentration enables the needed combination of high sensitivity, low LoD, and stable operation.

Pb-based perovskites add a further regulatory impediment to adoption [16–20]. Bismuth (Bi) is considered a promising candidate to replace Pb: it is not subject to the same RoHS regulations, yet also has a high atomic number [21,22]. Here we report ultrasensitive and stable X-ray detectors enabled by the utilization of solution-processed zero-dimensional (0D) lead-free $MA_3Bi_2I_9$ single crystals, which shows suppressed ion migration (activation energy for ion migration, $E_a = 0.46$ eV), a dark carrier concentrations of ~ 10^6 cm^{-3} and a Hall mobility of 70 cm^2 V^{-1} s^{-1}. We report X-ray detectors with a high sensitivity of 10,620 μC $Gy_{air}{}^{-1}$ cm^{-2} and an LoD of 0.62 nGy_{air} s^{-1}. The LoD achieved herein is ~20 times lower than the lowest LoD reported in literature (see Table S1). The 0D perovskite X-ray detectors exhibit stable operation even under high applied biases up to 120 V. No deterioration in detection performance was observed following an X-ray irradiation dose of ~23,800 mGy_{air} (under bias of 50 V for 1091.3 mGy_{air} and 100 V for 22,767.2 mGy_{air}), equivalent to > 200,000 times of the dose used in acquiring commercial X-ray chest radiographs.

2. Experimental

2.1. Materials

The materials used were as follows: bismuth triiodide (BiI_3) (99%, Sigma-Aldrich), methylamine (CH_3NH_2) (40% w/w aq. soln., Alfa Aesar), hydriodic acid (HI) (57% w/w aq. soln., Alfa Aesar), γ-butyrolactone (GBL) (>99%, Alfa Aesar), and diethyl ether (anhydrous, >99%, Alfa Aesar).

2.2. Synthesis of methylammonium iodide (MAI)

MAI was prepared by slowly adding hydroiodic acid into methylamine solution under continuous stirring at 0 °C for 3 h. MAI was crystallized by removing the solvent with a rotary evaporator. The MAI powder was then put into a Soxhlet extractor and repeatedly washed with diethyl ether overnight. The white, shiny crystals were dried under vacuum for 24 h and kept in a nitrogen glove box for further use.

2.3. Growth of $MA_3Bi_2I_9$ single crystal

First, 3 M MAI and 2 M BiI_3 were dissolved in GBL solution in a vial to keep the molar ratio of MAI to BiI_3 at 3:2. Then, the solution was heated and stirred at 60 °C on a hot plate for 12 h. The mixture was filtered with a PTFE filter (0.45 μm) before use. The $MA_3Bi_2I_9$ single crystal was grown using the seed-crystal-assisted constant-temperature evaporation method (SCA-CTEM). $MA_3Bi_2I_9$ single crystal seeds (1–2 mm in size) were obtained by keeping the precursor solution in a glass beaker at 60 °C for 24 h. Then, one crystal seed was placed into the fresh solution, which was heated and kept at 70 °C for a long period of time. A reddish black $MA_3Bi_2I_9$ crystal with a size of ~27 mm × 23 mm × 13 mm was obtained after 20 days of growth.

2.4. Cutting of the $MA_3Bi_2I_9$ single crystal

A large $MA_3Bi_2I_9$ single crystal was cut into slices with different thicknesses using a diamond wire saw (STX-202A, Shenyang Kejing Auto-Instrument Co., LTD). The diameter of the diamond wire was 0.125 mm. Isopropanol was used as the cooling liquid during the cutting process.

2.5. Characterization of materials

Powder XRD measurements of $MA_3Bi_2I_9$ were performed with an Empyrean X-ray diffractometer with Cu K_α radiation (PANalytical, 1°/min). $MA_3Bi_2I_9$ powders were obtained by grinding the single crystal. Humidity aging of the samples was carried out in a glass desiccator with a constant RH of ~60%. Thermogravimetric analysis (TGA) and differential scanning calorimetry (DSC) measurements were performed on a thermogravimetric analyzer (TGA/DSC 2, Mettler-Toledo, LLC) at a rate of 10 °C min^{-1} under a nitrogen atmosphere. UV−vis absorption spectra were recorded on an Evolution^{TM} 201 spectrophotometer (Thermo Fisher Scientific Corporation) in transmission mode using a $MA_3Bi_2I_9$ crystal slice (~0.5 mm).

2.6. Hall-effect measurement

A $MA_3Bi_2I_9$ single crystal with a size of 1.6 × 1.6 × 0.6 mm^3 was used for DC field Hall-effect measurement by van der Pauw method under high resistance mode (Lake Shore, 8400 series). Au evaporated on the four corners was used as the electrodes. The excitation current was 10 pA and the excitation magnetic field was 9 kG.

2.7. Hole and electron mobilities measured suing the time-of-flight (TOF) method

Gold (Au) charge-collecting electrodes with thicknesses of 10 nm and 80 nm were thermally evaporated on opposite sides of the $MA_3Bi_2I_9$ crystals, and the former was used as the semitransparent electrode for light transmission. The thicknesses of the $MA_3Bi_2I_9$ crystals were 0.88 mm and 1.10 mm for the out-of-plane and in-plane samples, respectively. TOF measurements were conducted by illuminating the devices with 6 ns width, 532 nm laser pulses on the 10 nm semitransparent Au electrode. The bias was applied to the sample using a function generator (DS345, Stanford Research Systems) and a Keithley digital source meter (model 2400). The photocurrent was recorded using a low-noise current preamplifier (SR570, Stanford Research Systems).

For hole mobility measurement, a 532 nm laser was illuminated on the 10 nm semitransparent Au cathode. The photogenerated holes traveled through the $MA_3Bi_2I_9$ single crystals under applied bias to reach the other electrode. For the electron mobility measurements, a 532 nm laser was illuminated on the 10 nm semitransparent Au anode. The photogenerated electrons traveled through the $MA_3Bi_2I_9$ single crystals under applied bias until reaching the other electrode. The charge carrier transit time (t_{tr}) was determined from the intercept of the pretransit and post-transit asymptotes of the photocurrent on a double logarithmic coordinate, as shown in Figs. S4–S7.

The mobility was calculated using the following formula:

$$\mu = \frac{d^2}{t_{tr}V}$$

where d is the thickness of the $MA_3Bi_2I_9$ single crystal, V the applied voltage, μ the charge carrier mobility and t_{tr} the transit time of the charge carriers.

2.8. X-ray tube equipment and dose rate calibration

Two kinds of homemade X-ray tubes used in this work were developed and produced by the Institute of Fluid Physics, CAEP. A relatively low-dose-rate (denoted by LDR) X-ray tube was used to study the detector performance. The LDR tube was designed for human medical X-ray CT with a small focal spot and excellent dose stability. The anode of the LDR tube is tungsten. The tube can be operated at voltages up to 140 kV, and the intrinsic filtration is equivalent to approximately 4.5 mm Al. Limited by the small focal spot, the LDR tube cannot continuously operate for a long period of time, especially at high X-ray dose rates.

A high-dose-rate (denoted by HDR) tube was used to study the radiation stability of the detector under continuous X-ray irradiation. The HDR tube was designed for X-ray irradiation research. The anode of the HDR tube is tungsten with cooling water, which can operate stably for several hours. The dose rate of the HDR tube can be adjusted by changing the tube current or distance between the detector and the tube. The highest dose rate can reach hundreds of mGy_{air} min^{-1}.

Dose rate calibrations of the tube were carried out by a Si dosimeter (model: RaySafe X2 R/F) from Fluke, which was operating in integrating mode. The dosimeter can monitor the voltage, exposure time and dose rate of the tube with excellent accuracy and stability. The dosimeter is calibrated annually by the National Institute of Measurement and Testing Technology by measuring the tube voltage and exposure time with a high-precision intervention high-voltage divider and time interval measuring instrument.

2.9. Photocurrent under X-ray exposure

The homemade LDR X-ray tube was used under an operating voltage of 100 kV. The dose rate was adjusted by changing the X-ray tube current as well as the location of the detector. The photocurrent of our Au/$MA_3Bi_2I_9$/Au device was recorded using a low-noise current preamplifier (SR570, Stanford Research Systems) under different bias voltages, which were applied by a function generator (DS345, Stanford Research Systems) and a Keithley digital source meter (model 2400). The thicknesses of the $MA_3Bi_2I_9$ single crystal and identical Au electrodes on both sides of the crystal are approximately 2.5 mm and 80 nm, respectively. The $\mu\tau$ product was fitted by the simplified Hecht equation:

$$J = J_0 \mu\tau V d^{-2}\left[1 - exp\left(-\frac{d^2}{\mu\tau V}\right)\right]$$

where J is the photocurrent density, J_0 is the saturated photocurrent density, V the applied bias and d the thickness of the single crystal.

2.10. X-ray response measurement

The devices with a configuration of Au/$MA_3Bi_2I_9$/Au were fabricated in both in-plane and out-of-plane transport mode for X-ray detection measurements. The approximately 2.5-mm-thick $MA_3Bi_2I_9$ acted as the active layer, and the Au layers (80 nm) acted as the electrodes. The I–t characteristics under various biases were measured by a low-noise current preamplifier (SR570, Stanford Research Systems). The homemade LDR X-ray tube was used as the X-ray source. The total X-ray dose was modulated by changing the current of the X-ray tube and the distance between the device and the X-ray source.

2.11. Stability characterization of the X-ray detector

The LDR tube was used to study the radiation stability of the detector under irradiation with an X-ray pulse (Fig. 4a, b). The HDR tube was used to study the radiation stability of the detector under continuous X-ray irradiation (Fig. 4c). $MA_3Bi_2I_9$ detectors without encapsulation working under different biases (50 and 100 V) were exposed to X-ray radiation under various dose rates (9.7, 38.2 and 152.8 mGy_{air} min^{-1}). The photocurrent was recorded during the X-ray radiation process.

2.12. Calculation of the signal-to-noise ratio

The signal current density (J_s) was derived by subtracting the average photocurrent density (J_p) by the average dark current density (J_d) using $J_s = J_p - J_d$. The noise current density (J_n) was obtained by calculating the standard deviation of the photocurrent density using the following expression:

$$J_n = \sqrt{\frac{1}{N}\sum_{i}^{N}(J_i - J_p)^2}$$

Then, the signal-to-noise ratio (SNR) was calculated by $SNR = J_s/J_n$.

Fig. S11 and Fig. 3b show the X-ray photoresponse characteristics of the in-plane device with a dose rate of 425 nGy_{air} s^{-1} and the out-of-plane device with a dose rate of 5.3 nGy_{air} s^{-1}. The J_s values were 0.141 nA cm^{-2} and 0.053 nA cm^{-2} for the in-plane and out-of-plane devices, respectively. The calculated average noise currents were 0.014 nA cm^{-2} and 0.006 nA cm^{-2}, resulting in SNR values of 9.8 and 8.8 for the in-plane and out-of-plane devices, respectively.

3. Results and discussion

3.1. Development of zero-dimensional perovskite single crystals

We grew 0D $MA_3Bi_2I_9$ perovskite single crystals using the seed-crystal-assisted constant-temperature evaporation method. $MA_3Bi_2I_9$ is a zero-dimensional material as illustrated in Fig. 1(a). The structure has hexagonal symmetry (P63/mmc) with face-sharing BiI_6 dioctahedral $(Bi_2I_9)^{3-}$ clusters isolated by MA^+. Unit-cell parameters of $a = b = 8.58$ Å and $c = 21.76$ Å are derived from the XRD patterns. The organic cations act as insulating spacing layers between the $(Bi_2I_9)^{3-}$ clusters, and the unique zero-dimensional characteristics of $MA_3Bi_2I_9$ offer promise on suppressing ion migration. The as-grown $MA_3Bi_2I_9$ crystal is of hexagonal shape (Fig. 1b shows a crystal with ~27 mm × 23 mm × 13 mm dimensions) and can endure temperatures up to 250 °C with no phase transition (Fig. S1). The $MA_3Bi_2I_9$ perovskite crystals exhibited no observable change in the X-ray diffraction (XRD) patterns after storage for 34 days in ambient air with a RH of ~60% (Fig. 1c).

The high-Z elements (Bi and I) and the high density (3.8 g cm^{-3}) favor a high X-ray absorption for $MA_3Bi_2I_9$ [8]. We compared the absorption coefficients (Fig. S2) and the attenuation efficiency of typical materials used for X-ray detection to 50 keV X-ray photons versus thickness (Fig. 1d). The absorption features of these materials were calculated according to the photon cross-section database [23]. The attenuation efficiency of $MA_3Bi_2I_9$ is similar to that of $Cs_2AgBiBr_6$ and is larger than that of a-Se and $MAPbBr_3$. We further measured the absorption spectra of a thin slice of $MA_3Bi_2I_9$ single crystal (Fig. S3), showing an optical band gap of 1.98 eV that lies in the range of room temperature operation for X-ray detectors [24].

3.2. Electronic properties of $MA_3Bi_2I_9$ single crystals

Although $MA_3Bi_2I_9$ exhibit zero dimensionality in crystalline structure, the $MA_3Bi_2I_9$ single crystals may exhibit anisotropy in electrical properties due to the different orientation arrangement of $(Bi_2I_9)^{3-}$ clusters along c-axis and a/b-axes. To investigate the anisotropic electrical properties of $MA_3Bi_2I_9$, we cut the crystal into a rectangle along the c axis (Fig. 2a). We measured the

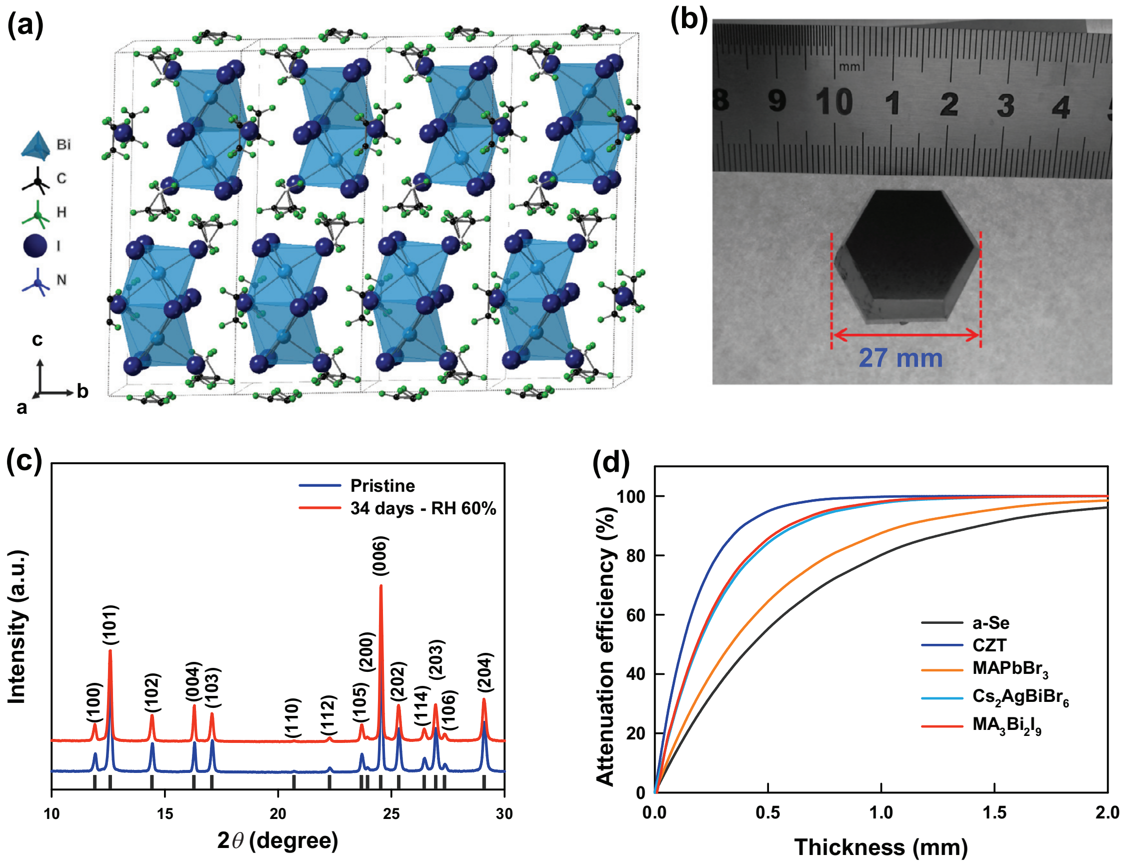

Fig. 1. Characterization of zero-dimensional (0D) $MA_3Bi_2I_9$ perovskite single crystals. (a) Crystal structure of 0D $MA_3Bi_2I_9$. (b) Photograph of a $MA_3Bi_2I_9$ crystal. (c) XRD patterns of pristine $MA_3Bi_2I_9$ powders and aged powder kept under relative humidity (RH) of 60% for 34 days. (d) Calculated attenuation efficiencies of a-Se, $Cd_{0.9}Zn_{0.1}Te$ (CZT), $MAPbBr_3$, $Cs_2AgBiBr_6$, and $MA_3Bi_2I_9$ semiconductors to 50 keV X-ray photons versus thickness.

in-plane (perpendicular to the c axis) resistivity and the out-of-plane (along the c axis) resistivity (Fig. 2b). The bulk resistivity in the out-of-plane direction reaches 5.27×10^{11} Ω cm and is approximately ten times higher than that in the in-plane direction (5.52×10^{10} Ω cm). The out-of-plane resistivity of $MA_3Bi_2I_9$ crystal is considerably higher than that of CZT crystal (10^{10} Ω cm) and other 3D perovskites (10^7–10^8 Ω cm) [25,26].

Hall-effect measurements were used to investigate the charge carrier mobility (μ) and dark carrier concentration in $MA_3Bi_2I_9$ crystals (see Experimental section). A bulk resistivity of 5×10^{10} Ω cm was obtained, is similar to that observed in the in-plane direction. $MA_3Bi_2I_9$ demonstrates p-type conduction with a mobility of 70 cm^2 V^{-1} s^{-1} and a carrier concentration of 1.6×10^6 cm^{-3}. The mobility is slightly inferior to that of 3D Pb-based perovskites, while the carrier concentration is several orders of magnitude lower than those reported in 3D perovskites (typically ~10^{12} cm^{-3}) [27]. The low carrier concentration in $MA_3Bi_2I_9$ can reduce the carrier scattering during the charge transporting process, which favors its high mobility.

We further studied the charge carrier mobility (μ) of $MA_3Bi_2I_9$ crystals by time-of-flight (TOF) at 50–210 V (Figs. S4–S7). The mobility shows a negative bias dependence due to the increased scattering at higher bias. The hole mobilities are 2–6 cm^2 V^{-1} s^{-1} in the in-plane direction and 1–4 cm^2 V^{-1} s^{-1} in the out-of-plane direction, and the electron mobilities are 4–8 cm^2 V^{-1} s^{-1} in the in-plane direction and 2–5 cm^2 V^{-1} s^{-1} in the out-of-plane direction (Fig. 2c, d). The quasi-balanced carrier mobilities indicate ambipolar transport in $MA_3Bi_2I_9$ crystals. We further derived the dark free carrier concentration (n) in the $MA_3Bi_2I_9$ crystal through $n = 1/\rho q\mu$, where ρ is the bulk resistivity and q is the elementary charge. The carrier concentration in $MA_3Bi_2I_9$ crystals lies within the range from 10^6–10^7 cm^{-3} (Table S2). The mobility and carrier concentration show a little difference with the data obtained using Hall-effect measurements, but once again demonstrates the high mobility and low carrier concentration features of $MA_3Bi_2I_9$ crystals.

We then measured the charge carrier mobility-lifetime ($\mu\tau$) product in $MA_3Bi_2I_9$ under various bias using photoconductivity method (Fig. S8). We employed a modified Hecht equation to fit the photoconductivity curve under X-ray excitation to obtain the $\mu\tau$ values (see Experimental section) [28]. The $\mu\tau$ products of 2.8×10^{-3} and 1.2×10^{-3} cm^2 V^{-1} were obtained for the in-plane and the out-of-plane directions, respectively (Fig. 2e, f). The $\mu\tau$ products in both directions are superior to those of CZT and HgI_2 semiconductors [25,29].

3.3. Performance of X-ray detectors

We fabricated direct-conversion X-ray detectors and characterized their performance using a device structure of Au/$MA_3Bi_2I_9$ single crystal/Au. The dark current density (J_d) plays a crucial role on the sensitivity and LoD of X-ray detectors. We measured the J_d of the Au/$MA_3Bi_2I_9$/Au X-ray detectors (Fig. 3a). The J_d in the out-of-plane direction is 0.98 nA cm^{-2} under an applied bias of 120 V, which is lower than that in the in-plane direction (28.4 nA cm^{-2}). The J_d maintained constant during the measurements and no obvious current drift was observed in either out-of-plane or in-plane direction (Fig. S9a, b). The stable outputs of J_d in-

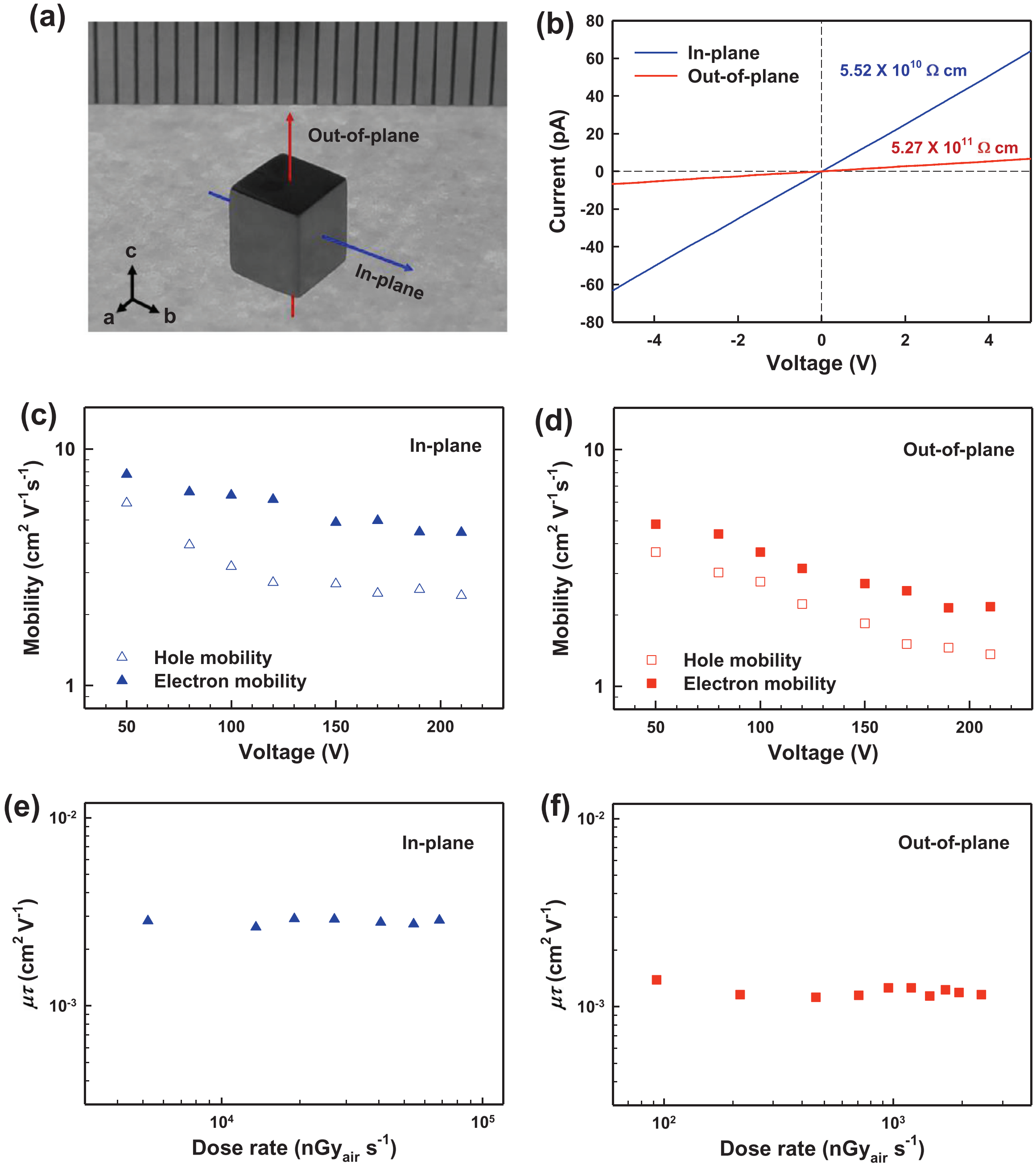

Fig. 2. Anisotropic electronic properties of $MA_3Bi_2I_9$ single crystals. (a) Photograph of the $MA_3Bi_2I_9$ single crystal after cutting and polishing; charge transport perpendicular to the *c* axis in hexagonal $MA_3Bi_2I_9$ was defined as in-plane and charge transport along the *c* axis was defined as out-of-plane. (b) Anisotropic resistivity of the $MA_3Bi_2I_9$ single crystal. (c, d) Charge carrier mobility in $MA_3Bi_2I_9$ single crystal of (c) in-plane and (d) out-of-plane measured by time-of-flight (TOF) technique. (e, f) Dose rate dependence of the charge carrier mobility-lifetime ($\mu\tau$) product for $MA_3Bi_2I_9$ single crystal in (e) in-plane and (f) out-of-plane transport mode.

dicate that ion migration in 0D $MA_3Bi_2I_9$ crystals is negligible in both directions. We evaluated the ionic conduction activation energy (E_a) by temperature-dependent conductivity measurements [30,32], and the E_a values were fitted to be 0.31 and 0.46 eV for the in-plane and out-of-plane directions, respectively (Fig. S10), higher than those reported for 3D $MAPbI_3$ and $MAPbBr_3$ (typically below 0.19 eV) [26,32].

The low and stable dark current enables us to observe stable and distinguishable signals in response to low X-ray radiation. When exposed to a dose rate of 5.3 nGy_{air} s^{-1}, the lowest value achievable in our X-ray generator, the out-of-plane devices exhibit a signal-to-noise ratio (SNR) of 8.8 (Fig. 3b, see Experimental section for details). The LoD of 0.62 nGy_{air} s^{-1} was linearly extrapolated from the X-ray dose rate-dependent SNR following the IUPAC standard with a SNR value of 3 (Fig. 3c). This LoD represents the lowest value reported for X-ray detectors (the lowest LoD reported previously was 36 nGy_{air} s^{-1} for direct-conversion X-ray detectors; Fig. 3(d), Table S1) [1,2,13,26,30,31,33]. Notably, the LoD of 0.62 nGyair s^{-1} for the out-of-plane devices approaches the background radiation on Earth (~0.1 nGyair s^{-1}) [11], and it is approximately 8,800 times lower than the dose rate required for X-ray diagnostics used currently (5.5 μGy_{air} s^{-1}) [33], offering the potential to further lower the radiation dose required for medical radiography, industrial inspection and security scanning.

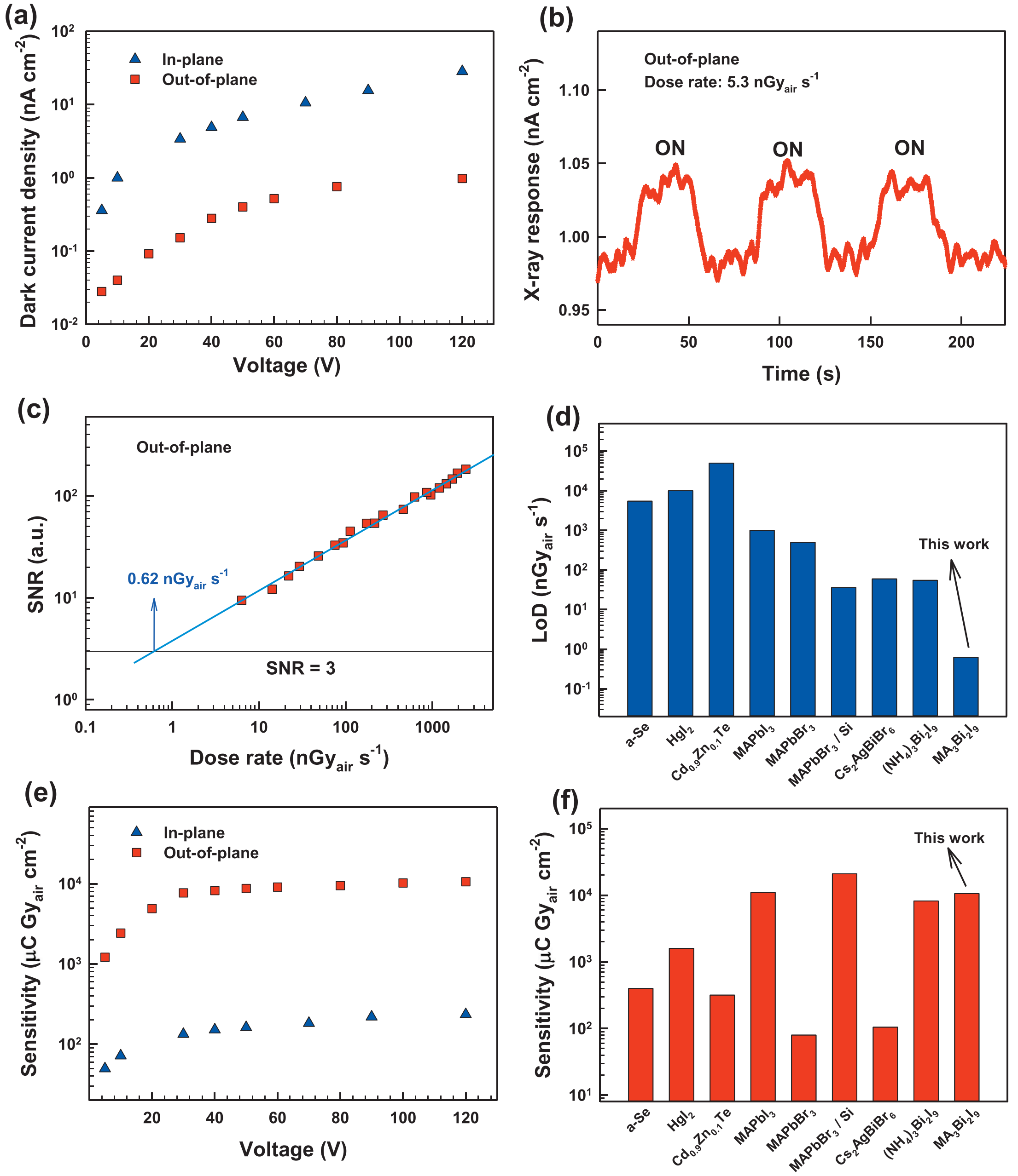

Fig. 3. Performance of $MA_3Bi_2I_9$ X-ray detectors. (a) Bias dependence of the dark current density (J_d) of Au/$MA_3Bi_2I_9$/Au device. (b) X-ray response characteristics for an out-of-plane device with a dose rate of 5.3 nGy$_{air}$ s^{-1}. (c) X-ray dose rate-dependent signal-to-noise ratio (SNR) of the out-of-plane device (40 V bias). The LoD of 0.62 nGy s^{-1} is derived from the slope of the fitting line with a signal-to-noise ratio of 3. (d) Comparison of LoD of various direct-conversion X-ray detectors [1,2,13,26,30,31]. (e) Bias-dependent X-ray sensitivity of the in-plane and out-of-plane devices. (f) Comparison of the best sensitivity in literature for direct-conversion X-ray detectors [1,2,13,26,30,31].

Fig. 3e presents the X-ray sensitivity of the in-plane and out-of-plane devices under various biases. The out-of-plane devices have a X-ray sensitivity of 10,620 μC Gy$_{air}$$^{-1}$ cm^{-2} at the operating bias of 120 V, which is about 50 times higher than the sensitivity in the in-plane devices. The out-of-plane sensitivity is comparable to the best values obtained by 3D perovskite (1.1 × 10^4 μC Gy$_{air}$$^{-1}$ cm^{-2} for $MAPbI_3$ and 2.1 × 10^4 μC Gy$_{air}$$^{-1}$ cm^{-2} for hybrid $MAPbBr_3$/Si) and 2D perovskite (8,400 μC Gy$_{air}$$^{-1}$ cm^{-2} for $(NH_4)_3Bi_2I_9$) X-ray detectors, but is higher than those of a-Se, CZT and $Cs_2AgBiBr_6$ (Fig. 3f, Table S1). It is worth noting that, unlike 2D hybrid Bi halide perovskites cannot achieved low LoD and high sensitivity in the same direction [30], 0D $MA_3Bi_2I_9$ X-ray detectors achieve simultaneously low LoD and high X-ray sensitivity in the same out-of-plane transport mode.

3.4. Operational stability of X-ray detectors

We finally investigated the operational stability of $MA_3Bi_2I_9$ X-ray detectors (in the out-of-plane direction) under ambient condition without encapsulation. The device was first exposed to X-ray radiation with a dose rate of 9.7 mGy$_{air}$ min^{-1} under a constant bias of 50 V for 225 pulses (Fig. 4a). Following a total X-ray dose of 1091.3 mGy$_{air}$, no observable change in SNR occurred in the detector (Fig. 4b). We then applied a higher working bias (100 V) and higher continuous X-ray dose rates (38.2 and 152.8 mGy$_{air}$ min^{-1}) to irradiate the detector, and no obvious change in photocurrent was found following an additional total X-ray dose of over 22,767.2 mGy$_{air}$ (Fig. 4c). This total dose is equivalent to ~230,000 times of the dose required for an X-ray chest

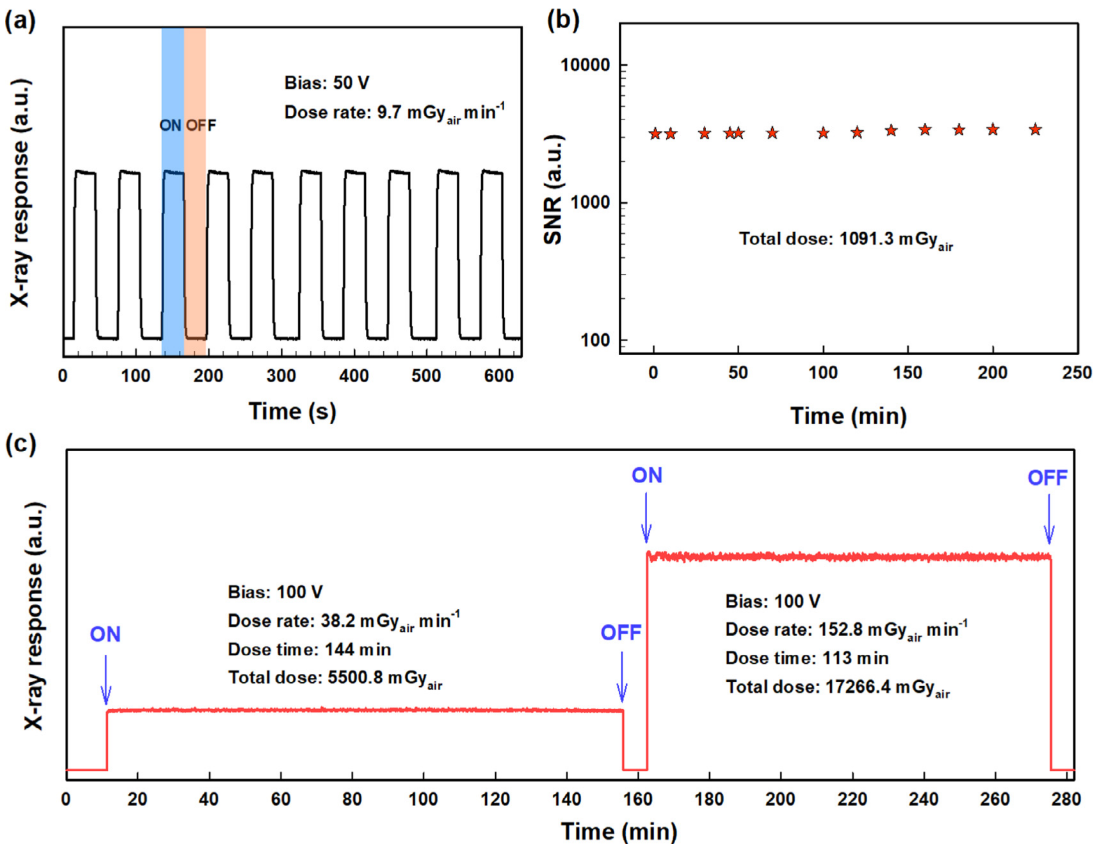

Fig. 4. Radiation stability of 0D $MA_3Bi_2I_9$ X-ray detectors (out-of-plane). (a, b) Device operational stability under X-ray pulses with a time interval of 30 s: (a) A portion of the device responses to X-ray pulses and (b) time-dependent SNR of the devices. (c) Device operational stability against continuous X-ray irradiation with high dose rates under a high bias voltage of 100 V. Radiation stability tests were performed in ambient air without encapsulation.

radiograph (typically ~0.1 mGy$_{air}$ for commercial instruments). This indicates that X-detectors using 0D $MA_3Bi_2I_9$ perovskites can guarantee reliable operation for medical radiography applications.

4. Conclusions

In summary, the 0D $MA_3Bi_2I_9$ perovskite single crystal presents high attenuation efficiency, a high $\mu\tau$ product, an ultralow carrier concentration, suppressed ion migration, and excellent thermal and ambient stability. These features endow the $MA_3Bi_2I_9$ devices with ultrasensitive and high stability X-ray detection. The X-ray detection limit of the $MA_3Bi_2I_9$ detectors down to 0.62 nGy$_{air}$ s^{-1} enables a reduction in the dosage required for regular X-ray inspection to a low level, enabling reduced health risks and more frequent diagnostic imaging assays. Moreover, the excellent operational stability under high bias and high X-ray dose more than 23,858.5 mGy$_{air}$ reveals its great value in practical application. Our results pave a way of exploring ultrasensitive and stable X-ray detectors.

Author contributions

X.Z. and W-H.Z. conceived the idea and designed the experiments. W-H.Z., and J.L. led the collaboration efforts. P.W. prepared the perovskite single crystals. X.Z. and T.S. performed the structural and optoelectronic characterization of the perovskites. H.T. and M.I.S. helped on the growth of single crystals and characterization. X.Z. and T.S. fabricated the detector. W.Z., X.Z. designed and carried out the detector performance characterization with the supervision of J.L.. W.Z., S.T. and L.C. carried out the stability characterization. Y. P. and W.Z. prepared the X-ray sources and carried out the dose calibrations. X.Z., H.T., W.Z., M.I.S. and W-H.Z. wrote the manuscript. All authors discussed the results and commented on the manuscript.

Declaration of competing interests

The authors declared that they have no conflicts of interest to this work.

Acknowledgments

We thank Edward H. Sargent from University of Toronto for discussions and revising of the manuscript. We also thank Jianbei Li, Zhen Qin and Ping Liu from the Institute of Fluid Physics, CAEP, for technical assistance. This work is supported by the National Natural Science Foundation of China (Grant nos. 21773218, 61974063), the Sichuan Province (Grant no. 2018JY0206) and the China Academy of Engineering Physics (Grant no. YZJJLX2018007).

Data availability

The data sets analyzed during the study are available from the corresponding authors upon request. Correspondence and requests for materials should be addressed to W.-H. Z. (whzhang@caep.cn) or J.L. (longjidong@tsinghua.org.cn).

Supplementary materials

Supplementary materials associated with this article can be found, in the online version, at doi:10.1016/j.jechem.2020.02.049.

References

[1] H. Wei, Y. Fang, P. Mulligan, W. Chuirazzi, H.-H. Fang, C. Wang, B.R. Ecker, Y. Gao, M.A. Loi, L. Cao, J. Huang, Nat. Photon. 10 (2016) 333–339.
[2] W. Wei, Y. Zhang, Q. Xu, H. Wei, Y. Fang, Q. Wang, Y. Deng, T. Li, A. Gruverman, L. Cao, J. Huang, Nat. Photon. 11 (2017) 315–321.
[3] J.A. Rowlands, Nature 550 (2017) 47–48.
[4] Y.C. Kim, K.H. Kim, D.-Y. Son, D.-N. Jeong, J.-Y. Seo, Y.S. Choi, I.T. Han, S.Y. Lee, N.-G. Park, Nature 550 (2017) 87–91.
[5] D.M. Panneerselvam, M.Z. Kabir, J. Mater. Sci-Mater El 28 (2017) 7083–7090.
[6] G. Zentai, L.D. Partain, R. Pavlyuchkova, C. Proano, G.F. Virshup, B.N. Breen, A.I. Vilensky, O. Dagan, E. Meerson, M. Schieber, H. Gilboa, J.A. Thomas, Detailed imager evaluation and unique applications of a new 20cmx25-cm size mercuric iodide thick film x-ray detector, Proceedings of SPIE2003.
[7] H.M. Thirimanne, K.D.G.I. Jayawardena, A.J. Parnell, R.M.I. Bandara, A. Karalasingam, S. Pani, J.E. Huerdler, D.G. Lidzey, S.F. Tedde, A. Nisbet, C.A. Mills, S.R.P. Silva, Nat. Commun. 9 (2018) 2926.
[8] S. Yakunin, M. Sytnyk, D. Kriegner, S. Shrestha, M. Richter, G.J. Matt, H. Azimi, C.J. Brabec, J. Stangl, M.V. Kovalenko, W. Heiss, Nat. Photon. 9 (2015) 444–449.
[9] Y. Rong, Y. Hu, A. Mei, H. Tan, M.I. Saidaminov, S.I. Seok, M.D. McGehee, E.H. Sargent, H. Han, Science 361 (2018) eaat8235.
[10] C.C. Stoumpos, M.G. Kanatzidis, Adv. Mater. 28 (2016) 5778–5793.
[11] H. Wei, J. Huang, Nat. Commun. 10 (2019) 1066.
[12] S. Shrestha, R. Fischer, G.J. Matt, P. Feldner, T. Michel, A. Osvet, I. Levchuk, B. Merle, S. Golkar, H. Chen, S.F. Tedde, O. Schmidt, R. Hock, M. Rührig, M. Göken, W. Heiss, G. Anton, C.J. Brabec, Nat. Photon. 11 (2017) 436.
[13] B. Yang, W. Pan, H. Wu, G. Niu, J.-H. Yuan, K.-H. Xue, L. Yin, X. Du, X.-S. Miao, X. Yang, Q. Xie, J. Tang, Nat Commun 10 (2019) 1989.
[14] V. Morad, Y. Shynkarenko, S. Yakunin, A. Brumberg, R.D. Schaller, M.V. Kovalenko, J. Am. Chem. Soc. 141 (2019) 9764–9768.
[15] S. Yakunin, B.M. Benin, Y. Shynkarenko, O. Nazarenko, M.I. Bodnarchuk, D.N. Dirin, C. Hofer, S. Cattaneo, M.V. Kovalenko, Nat. Mater. 18 (2019) 846–852.
[16] A. Babayigit, A. Ethirajan, M. Muller, B. Conings, Nat. Mater. 15 (2016) 247–251.
[17] W. Ning, F. Wang, B. Wu, J. Lu, Z. Yan, X. Liu, Y. Tao, J.M. Liu, W. Huang, M. Fahlman, L. Hultman, T.C. Sum, F. Gao, Adv. Mater. 30 (2018) 1706246.
[18] Y. Liao, H. Liu, W. Zhou, D. Yang, Y. Shang, Z. Shi, B. Li, X. Jiang, L. Zhang, L.N. Quan, R. Quintero-Bermudez, B.R. Sutherland, Q. Mi, E.H. Sargent, Z. Ning, J. Am. Chem. Soc. 139 (2017) 6693–6699.
[19] M. Chen, M.-G. Ju, A.D. Carl, Y. Zong, R.L. Grimm, J. Gu, X.C. Zeng, Y. Zhou, N.P. Padture, Joule 2 (2018) 558–570.
[20] J.-P. Correa-Baena, M. Saliba, T. Buonassisi, M. Grätzel, A. Abate, W. Tress, A. Hagfeldt, Science 358 (2017) 739–744.
[21] R. Mohan, Nat. Chem. 2 (2010) 336 -336.
[22] W. Yuan, G. Niu, Y. Xian, H. Wu, H. Wang, H. Yin, P. Liu, W. Li, J. Fan, Adv. Funct. Mater. 29 (2019) 1900234.
[23] M.J. Berger, J.H. Hubbell, S.M. Seltzer, J. Chang, J.S. Coursey, R. Sukumar, D.S. Zucker, K. Olsen, NIST (2010).
[24] D.S. McGregor, H. Hermon, Nucl. Instrum. Meth. A 395 (1997) 101–124.
[25] S. Del Sordo, L. Abbene, E. Caroli, A.M. Mancini, A. Zappettini, P. Ubertini, Sensors 9 (2009) 3491–3526.
[26] W. Pan, H. Wu, J. Luo, Z. Deng, C. Ge, C. Chen, X. Jiang, W.-J. Yin, G. Niu, L. Zhu, L. Yin, Y. Zhou, Q. Xie, X. Ke, M. Sui, J. Tang, Nat. Photon. 11 (2017) 726.
[27] Y. Liu, Z. Yang, D. Cui, X. Ren, J. Sun, X. Liu, J. Zhang, Q. Wei, H. Fan, F. Yu, X. Zhang, C. Zhao, S. Liu, Adv. Mater. 27 (2015) 5176–5183.
[28] S. Yakunin, D.N. Dirin, Y. Shynkarenko, V. Morad, I. Cherniukh, O. Nazarenko, D. Kreil, T. Nauser, M.V. Kovalenko, Nat. Photon. 10 (2016) 585–589.
[29] B.D. Milbrath, A.J. Peurrung, M. Bliss, W.J. Weber, J. Mater. Res. 23 (2011) 2561–2581.
[30] R. Zhuang, X. Wang, W. Ma, Y. Wu, X. Chen, L. Tang, H. Zhu, J. Liu, L. Wu, W. Zhou, X. Liu, Y. Yang, Nat. Photon. 13 (2019) 602–608.
[31] G. Zentai, L. Partain, R. Pavlyuchkova, C. Proano, G. Virshup, L. Melekhov, LE (Ed.), PTS 1 AND 2N DIEGO, CA, 2003, pp. 77–91.
[32] Y. Lin, Y. Bai, Y. Fang, Q. Wang, Y. Deng, J. Huang, ACS Energy Lett. 2 (2017) 1571–1572.
[33] Q. Chen, J. Wu, X. Ou, B. Huang, J. Almutlaq, A.A. Zhumekenov, X. Guan, S. Han, L. Liang, Z. Yi, J. Li, X. Xie, Y. Wang, Y. Li, D. Fan, D.B.L. Teh, A.H. All, O.F. Mohammed, O.M. Bakr, T. Wu, M. Bettinelli, H. Yang, W. Huang, X. Liu, Nature 561 (2018) 88–93.